Interhemispheric asymmetry of climate change projections of boreal winter surface winds in CanESM5 large ensemble simulations

Bin Yu (Bin.Yu@canada.ca)
Environment and Climate Change Canada https://orcid.org/0000-0002-3706-8194
Xuebin Zhang
ECCC
Guilong Li
ECCC-ECCC: Environment and Climate Change Canada
Wei Yu
ECCC-ECCC: Environment and Climate Change Canada

Research Article

Keywords: Future projections, surface mean and extreme winds, SMILE, CanESM5

Posted Date: May 19th, 2021

DOI: https://doi.org/10.21203/rs.3.rs-476108/v1

Version of Record: A version of this preprint was published at Climatic Change on February 1st, 2022. See the published version at https://doi.org/10.1007/s10584-022-03313-2.

Interhemispheric asymmetry of climate change projections of boreal winter surface winds in CanESM5 large ensemble simulations

Abstract

A recent study of future changes in global wind power using an ensemble of ten CMIP5 climate simulations indicated an interhemispheric asymmetry of wind power changes over the 21st century, featured by power decreases across the Northern Hemisphere mid-latitudes and increases across the tropics and subtropics of the Southern Hemisphere. Here we analyze future global projections of surface mean and extreme winds by means of a single-model initial-condition 50-member ensemble of climate simulations generated with CanESM5, the Canadian model participated in CMIP6. We analyze the ensemble mean and spread of boreal winter mean and extreme wind trends over the next half-century (2021-2070) and explore the contribution of internal climate variability to these trends. Surface wind speed is projected to mostly decrease in northern mid-low latitudes and southern mid-latitudes and increase in northern high latitudes and southern tropical and subtropical regions, with considerable regional variations. Large ensemble spreads are apparent, especially with remarkable differences over northern parts of South America and northern Russia. The interhemispheric asymmetry of wind projections is found in most ensemble members, and can be related to large-scale changes in surface temperature and atmospheric circulation. The extreme wind has similar structure of future projections, whereas its reductions tend to be more consistent over northern mid-latitudes. The projected mean and extreme wind changes are attributed to changes in both externally anthropogenic forced and internal climate variability generated components. The spread in wind projections is partially due to large-scale atmospheric circulation variability.

Key words: Future projections, surface mean and extreme winds, SMILE, CanESM5

1. Introduction

Wind power is a sustainable and renewable source of energy that contributes significantly to reduce global greenhouse gas emissions and affects the Earth's climate (e.g., Solomon et al., 2007). Wind energy production depends on weather conditions and is therefore influenced by climate variability and climate changes. In particular, climate variability and changes could alter the spatial and temporal characteristics of wind patterns by means of changes in the background climatological condition and synoptic-scale variation. Wind power is defined as the kinetic energy of air in motion and mainly depends on wind speed, although it is also influenced by air density that is a function of pressure, temperature and humidity. Given that wind power is the cube of wind speed, a small change in wind can have substantial consequences for the wind energy (e.g., Pryor and Barthelmie, 2010). For example, a 10% of wind change could bring about 30% of wind energy density change. Hence, understanding the influence of climate variability and future climate changes on wind is a crucial aspect in the wind resource study.

Wind energy is produced from wind to mechanical power through wind turbines. Wind speed normally increases with altitude and over open areas without windbreaks. At current stage, the most popular height of wind turbine is about 80 meters above ground level. In relevant observational and modeling studies, winds have been considered at various levels and the wind speed profile is usually represented by the theoretical power-law profile (e.g., Hsu et al., 1994; McVicar et al. 2008; Kim and Paik, 2015). For example, wind speeds at near-surface levels (typically at 10 m above the surface) and the free troposphere (such as 850 hPa and 300 hPa) have been employed in studies of the wind trend (e.g., Pryor et al., 2009; Vautard et al., 2010; McVicar et al., 2012; Torralba et al., 2017). Winds at the free atmosphere are considered to reduce the influence of surface geophysical fields so that less uncertainty can be expected in the wind speed estimation. In general, a broadly similar pattern of the wind trend in past few decades can be

obtained at various levels, suggesting that the main driver of the wind speed trend tends to be the change in large-scale atmospheric circulation (Torralba et al., 2017).

Wind changes have been extensively investigated on regional and local scales (e.g., reviews of Pryor and Barthelmie, 2010, and Wu et al., 2018, and references therein; Karnauskas et al., 2018). These involve studies of surface wind changes in past decades (e.g., Klink, 1999; Pryor et al., 2009; McVicar and Roderick, 2010; Vautard et al., 2010; McVicar et al., 2010, 2012; Bett et al., 2017; Zeng et al., 2018) and future wind projections (e.g., Pryor et al., 2010; Hueging et al., 2012; Kumar et al., 2014; Reyers et al., 2016; Moemken et al., 2018). However, few studies have focused on a global scale. Recently, Karnauskas et al. (2018) performed a global assessment of future changes in wind power using an ensemble of climate simulations from 10 models (one integration for each model) participated in the Coupled Model Intercomparison Project Phase 5 (CMIP5). An interhemispheric asymmetry of wind power changes over the coming century, featured by decreases across the Northern Hemisphere (NH) mid-latitudes and increases across the tropics and subtropics of the Southern Hemisphere (SH), was found. They also pointed out that the wind power change can be partially explained by established features of global warming, particularly the projected change of temperature gradients related to polar amplification in high latitudes and land amplification in low latitudes. The interhemispheric asymmetry of future wind changes can be schematically illustrated in Fig. 1. This figure shows zonal averages of northern wintertime surface air temperature changes for the periods over 2001-2050 and 2051-2100 relative to 1951-2000 (left panel in Fig.1), based on the Canadian Earth System Model version 5 (CanESM5) climate simulations, which reveals a signature of poleward amplification. The projected temperature changes can be simplified by fourth order polynomial fits. The interhemispheric asymmetry feature of wind changes can be schematically illustrated by the projected geostrophic wind approximations in both periods (right panel in Fig.1), calculated from the quartic fit curves of temperature changes.

This indicates the driving force of air temperature on wind changes. Of course, the geostrophic wind differs from real wind near the surface where winds are highly influenced by the friction force, as will be discussed further in section 3. In addition, the contribution of internal climate variability to climate changes of temperature and precipitation has been found to be comparable to their externally anthropogenic forced counterparts on regional scales (e.g., Deser et al., 2012, 2014; Yu et al., 2020). Whether the interhemispheric asymmetry of future wind changes can be found in climate projections simulated by state-of-the-art climate models participated in the Coupled Model Intercomparison Project Phase 6 (CMIP6) of the World Climate Research Programme, and to what extent the wind change is influenced by internal climate variability are important issues that wait to be addressed.

The purpose of this study is to explore the global projection of surface wind over the next half-century as well as the role of internal variability on this projection, by means of a 50-member ensemble of climate simulations generated by CanESM5 that is the Canadian model participating in CMIP6. Single model initial-condition large ensemble (SMILE) simulations enable us to make a robust quantification of projections and to isolate the internal climate variability generated component from the externally forced response (e.g., Wallace et al., 2014; Deser et al., 2014; Kay et al., 2015). We examine global surface mean and extreme winds in boreal winter, at which the seasonal mean and variation of wind in the NH are stronger than those in other seasons (e.g., Peixoto and Oort, 1992). In particular, we would like to know if there is an interhemispheric asymmetry of wind projections in CanESM5 climate change simulations and how the asymmetry feature is influenced by internal climate variability. In addition, what are the differences in projected mean and extreme wind changes attributed to externally anthropogenic forcings and internal climate variability?

The rest of the paper is organized as follows: Section 2 describes the reanalysis data, CanESM5 model and simulations, and analysis methods employed. Section 3 evaluates the model performance of CanESM5 in simulating surface wind and examines the projected trend of surface wind over the next half-century, inter-member trend variance, forced and internal components of the trend, and contribution of large-scale atmospheric circulation variability on the trend. Section 4 describes the corresponding results as in Section 3 but for extreme wind. In addition, the driving force of air temperature on projected wind changes is also assessed in Section 3. A summary and discussion are given in section 5.

2. Data and Methodology

a. Reanalysis data

To evaluate the performance of CanESM5 in simulating surface wind, we compare the simulated and reanalysis based winds. Only horizontal components of surface winds over land are considered in this study. The daily near-surface wind speed (U at about 10m) data are extracted from the fifth generation of atmospheric reanalysis (ERA5, Hersbach et al., 2020) of the European Centre for Medium-Range Weather Forecasts (ECMWF). Ramon et al. (2019) compared surface winds in five state-of-the-art reanalyses and found that ERA5 outperforms the others in reproducing the observed mean and variability of surface winds on a daily time-scale. Here we use the bias corrected ERA5 data (Lange, 2019) and interpolate the data to standard 2.5° × 2.5° grids to compare with climate simulations. We also create an extreme wind index (U90) with the percentage of time when daily surface wind speed is above its 90^{th} percentile. The percentile-based index is derived using 1981-2010 as the base period and applying a 5-day running window. The extreme wind is then examined on a seasonal basis, like previous studies on extreme temperatures (e.g., Sillmann et al., 2013; Yu et al., 2021). We use 35 December-February (DJF) mean U and

extreme index U90 over 1980-2014 as the observed climatological means. Years refer to the January dates throughout this study.

b. CanESM5 simulations

Outputs from a large ensemble of historical and climate change forced simulations conducted with CanESM5 are employed. CanESM5 is a fully coupled ocean-atmosphere-land-sea ice climate model (Swart et al., 2019, and references therein) developed at the Canadian Centre for Climate Modelling and Analysis (CCCma). It has a horizontal T63 spectral resolution of approximately 2.8° in the atmosphere and roughly 1° in the ocean. Detailed descriptions of the model can be found on the website http://climate-modelling.canada.ca/climatemodeldata/data.shtml. The SMILE simulations we analyzed consist of 50 ensemble members of 251-yr integrations over the 1850-2100 period, with slightly different initial conditions for each run in 1850. Each of the simulations is forced by identical historical anthropogenic and natural forcings over the 1850-2014 period and by the shared socioeconomic pathway SSP5-8.5 scenario (Eyring et al., 2016) for the climate change simulation over 2015-2100. Owing to their design, differences between individual realizations are due solely to internally generated climate variability (Wallace et al., 2014; Deser et al., 2014).

The daily and monthly near-surface (10m) wind speeds in the historical and climate change simulations are employed. The simulated extreme index U90 is created using 1961-1990 as the base period. 1961-1990 is used here as the base to be consistent with extreme temperature and precipitation indices as defined and analyzed for these climate simulations (e.g., Yu et al., 2020, 2021). Nevertheless, the results reported below are nearly identical if we use 1981-2010 as the base period. In addition, the monthly surface air temperature (SAT) and sea level pressure (SLP) in the climate simulations are employed. The modelled mean and extreme winds in the historical simulation over 1980-2014 are compared to the corresponding ERA5 results to evaluate the model

performance. The projected wind trends over the next half-century are calculated using the climate change simulation over 2021-2070. The modelled variables we considered are interpolated to 2.5° × 2.5° grids.

c. Analysis methods

All analyses are based on DJF means of variables considered. The secular trend for the time series of interest is computed using a least squares method. The high order variation components of temperature and wind changes are calculated using normalized orthogonal polynomial approximations (e.g., Hildebrand 1956). The multi-member ensemble mean (EnM) quantity is obtained by averaging the statistics of individual members, i.e. the average of results from the 50 members. Following Deser et al. (2014), we partition the projected trend (X_{Total}) into externally anthropogenic forced (X_{Forced}) and internal climate variability generated ($X_{Internal}$) components:

$$X_{Total}(i) = X_{Forced}(i) + X_{Internal}(i) = X_{EnM} + X_{Internal}(i), \quad (1)$$

where i refers to an individual ensemble member and $i=1,\ldots,50$. X_{Forced} is estimated by averaging the projected trends over the 50 members (i.e., the EnM trend X_{EnM}), whereas $X_{Internal}$ is obtained by subtracting X_{Forced} from X_{Total}. In addition, a dynamical adjustment method is utilized to confirm the influence of large-scale circulation-induced variability on wind projections. Briefly, we characterize dominant modes of the inter-member variability of large-scale circulations by performing an empirical orthogonal function (EOF) analysis of the 50 projected SLP trends over 2021-2070. The three leading SLP predictors are determined for wind trends using the method of partial least squares. The dynamically adjusted trend is then obtained by removing the influence of these three orthogonal SLP predictor patterns in the wind trend.

The relative agreement of spatial wind patterns for individual members with the ERA5 reanalysis or EnM result is assessed by examining second-order pattern difference statistics and is illustrated in a BLT diagram (Boer and Lambert, 2001). A BLT diagram is a modified Taylor

diagram, which displays the pattern correlation, the ratio of model to ERA5 or EnM variances, and the relative mean square difference between each ensemble member and ERA5 or EnM quantities. In addition, as in Deser et al. (2012) and Chen and Yu (2020), EnM values that are significantly different from zero at the 95% confidence level relative to the spread of the 50 individual results are assessed by the criterion:

$$|EnM| \geq \frac{2\times STD}{\sqrt{N-1}}, \quad (2)$$

where $|EnM|$ is the absolute value of the EnM, STD the standard deviation of anomalies relative to the EnM of the 50 members, and $N=50$.

The geostrophic flow is a theoretical wind resulting from the balance between the pressure gradient force and the Coriolis force, which typically occurs above boundary friction layer in mid-latitudes. Using the ideal gas law, horizontal components of the geostrophic wind (u_g, v_g) can be approximated as:

$$u_g = -\frac{R}{f}\frac{\partial T}{\partial y}, \quad (3)$$

$$v_g = \frac{R}{f}\frac{\partial T}{\partial x}, \quad (4)$$

where $R=287$ Jdeg^{-1}kg^{-1} is the gas constant for dry air, $f = 2\Omega \sin \varphi$ the Coriolis parameter varying with latitude φ, $\Omega = 7.292 \times 10^{-5}$ rad s^{-1} the angular velocity of rotation for the earth, and T the air temperature. We calculate the idealized geostrophic wind change using SAT projections to assess the driving force of air temperature on wind changes.

3. Surface wind

a. Climatological mean

Figure 2 (left panels) displays the DJF climatological means of surface wind speed over the 1980-2014 period for the EnM of CanESM5 historical simulations and the ERA5 reanalysis. Strong wind speeds, with values exceeding 4 m/s, mainly appear over the central US, northern Canada,

Greenland, Sahara, Middle East, Central Asia, the Tibetan Plateau, northern Russia, Argentina, South Africa, and western-central Australia. Broadly similar patterns are seen in the EnM and ERA5, with a pattern correlation of 0.76 over land within the domain (60°S-80°N) of interest. However, the wind pattern is smoother in the EnM than ERA5, likely due to the multi-member average. The difference between them (EnM-ERA5, Fig.2, top right) is mostly apparent in magnitude of the wind, especially in those regions with high topographies such as the Tibetan Plateau, Rocky Mountains, Sahel, and Atacama Desert. Similar model biases are also found in sea-level pressure (Swart et al., 2019). The wind pattern seen in EnM is robust for all ensemble members. Fig.2 (bottom right) also shows the relative agreement of the climatological mean winds for individual members relative to the ERA5 result using a BLT diagram. The pattern correlations are 0.75-0.77 for the 50 members. Meanwhile, all members simulate slightly higher spatial variances compared to ERA5, which can be seen from the ratio of model to ERA5 variances (about 110%). The distinction between individual members is hence hardly discernible in the diagram. The mean square difference between model and reanalysis based patterns is about 50%, as distributed in the wind speed difference described above. Overall, the ERA5 based wind speed pattern is reasonably well simulated by CanESM5.

The discrepancy between the EnM and ERA5 may result from differences in the configuration and physics of the CanESM5 and ERA5 reanalysis models. In particular, the difference can be partially attributed to differences in the land-surface roughness and elevation representation. As demonstrated in previous studies (e.g., Ramon et al., 2019), the grid resolution of climate/reanalysis models has a significant influence on the surface roughness and elevation representation. Coarser resolution models tend to simulate stronger wind speeds over high-elevated mountain ranges. This applies to the difference between CanESM5 and ERA5. CanESM5 has a horizontal resolution of approximately 2.8° in the atmosphere (about 222 km at 45° of latitude), whereas ERA5 has a high

resolution of 31 km. Stronger winds are apparent over high mountain regions in CanESM5 than ERA5 (Fig.2, top right). Nevertheless, the model bias will be partly removed when using individual integrations to calculate climate change trends (e.g., Yu et al., 2020, 2021).

b. Projected trend

Figure 3 (top left) shows the ensemble mean of normalized surface wind speed trends over the 2021-2070 period. Here we normalize the wind trend at each grid by its climatological mean over 1951-2000 to make global trends more comparable to each other. In terms of the inter-member agreement according to Eq. (2), surface wind speed over the next half-century is projected to mostly decrease in the NH mid-low latitudes and SH mid-latitudes and increase in the NH high latitudes and SH tropical and subtropical regions, with considerable regional variations. Specifically, significant reductions with the trend value lower than -5%/50yr are found over western Canada, the northwestern and eastern US, central Greenland, northern Europe, middle parts of Central and South Asia, Kamchatka, parts of the western coast of South America, most of Central and South Africa, and parts of northeastern Australia. By contrast, remarkable increases with values exceeding 5%/50yr are found over most of the Canadian Arctic Archipelago, western Greenland, northern Russia, southern India and northwestern Indochina, south of West Africa, western and eastern Brazil, the subtropical Brazil, Angola, Tanzania, and Mozambique. Consequently, the zonal average of the trend is dominated by wind decreases over northern mid-low latitudes and southern mid-latitudes, accompanied by increases over northern high latitudes and southern tropical and subtropical regions (Fig.3, top right). The broad wind reductions over northern mid-latitude regions and increases across tropical and southern subtropical regions feature an interhemispheric asymmetry, as illustrated by a quartic fit on the zonal average (red curve in top right of Fig.3). The interhemispheric asymmetry feature apparent in the EnM of CanESM5 future wind projections generally resembles the result of Karnauskas et al. (2018), obtained from an ensemble of 10 CMIP5

climate change simulations. However, differences of regional wind projections, especially changes in tropical regions, are evident between them (cf. top panels in Fig.3 with Fig.3 in Karnauskas et al., 2018). The discrepancy may result from differences in climate models considered, as well as the ensemble number and external forcing used.

The spread of the normalized wind trends in CanESM5 simulations can be quantified by the standard deviation (STD) of trends across the 50 ensemble members. The inter-member variability (Fig.3, middle left) reveals a broadly uniform structure, with values about 3-6%/50yr, especially over northern mid-latitudes. Nevertheless, relatively low variances (below 3%/50yr) are apparent over northern low latitudes and southern mid-latitudes, whereas high variances exceeding 6%/50yr are seen over western Brazil and northern Russia, which contribute to relatively high zonal averages of variation in those latitudes (Fig.3, middle right). Figure 4 (left) further compares projected patterns of the wind trend in individual members to the EnM. The pattern correlations over the global land range from 0.71 to 0.91, indicating a broad similarity of the wind projections across the 50 members. However, the ensemble members have slightly higher spatial variances compared to the EnM, with the ratio of variances ranging from 105-135%. In addition, the mean square difference between each simulation and the EnM is about 25-50% for most members. These suggest diversities, in terms of magnitude and spatial structure of the projected trend, also appear across the ensemble members.

The relative contributions of external forcing and internal variability to the projected wind trend can be measured by the signal-to-noise ratio (SNR) of the ensemble mean trend to STD of trend. The SNR pattern (Fig.3, bottom panel) bears resemblance to the ensemble mean of the wind trend. Thus, the surface wind response to external forcings tends to be more detectable over those regions with significant changes of wind speed as described above (Fig.3, top left).

c. Internally generated and dynamically adjusted trends

The projected wind speed trend is further partitioned into externally forced and internal climate variability generated components, as indicated in Eq. (1). The forced trend is estimated by the EnM trend discussed above. The internally generated components of the wind trend in the 50 ensemble members reveal large diversities. Member 02 (M02) has the highest pattern correlation of the total trend (r=0.91) with the EnM, while member 28 (M28) has the lowest correlation (r=0.71). Fig. 5 presents the total and internally generated trends for these two members. For the total trend (Fig. 5, top panels), the two cases exhibit broadly similar structure, with a spatial correlation of 0.69 between them. However, notable differences between them are also found. In particular, opposite trends are apparent in northern parts of South America and central parts of North America. Meanwhile, differences in trend magnitude are evident, especially over northern Russia, South Asia and Central Africa. In addition, the interhemispheric asymmetry of wind projections can be seen in M02 but not in M28 (Fig.5, top right), since decreases of the wind trend dominate southern tropical and subtropical regions in M28. The difference between M02 and M28 is also clearly evident in the internally generated component (Fig. 5, bottom panels). The internal trend reveals large-scale spatial coherence rather than small-scale noise structure, similar to the feature seen in temperature projections (e.g., Deser et al., 2014; Yu et al., 2021). However, the pattern correlation of the internal trend between M02 and M28 is low (r=0.11), owing to substantial regional variations of the trend. In addition, the magnitude of the internal trend is comparable to the forced trend, apparent in spatial structure of the trends as well as their zonal averages (cf. bottom panels in Fig.5 with top panels in Fig.3).

The interhemispheric asymmetry of wind projections can be seen in about three-fourths of the 50 members (not shown). However, differences in total and internal trends are also found between individual members, especially over northern parts of South America and northern Russia, as would be expected from the inter-member variability of trend (Fig.3, middle panels). Therefore,

both the externally forced and internally generated components contribute noticeably to the projected wind trend.

The large-scale atmospheric circulation influences surface wind speed (e.g., Pryor et al. 2006; Vautard et al., 2010; Wu et al., 2018; Zeng et al., 2019). The circulation-induced variability is also found to play an important role in climate change projections (e.g., Deser et al., 2012, 2014; Holmes et al., 2016; Yu et al., 2021). To assess the impact of large-scale circulation-induced variability on the wind speed trend, we perform an EOF analysis on the SLP trends over 2021-2070 across the 50 ensemble members, within the 60ºS-80ºN domain involving land and oceans. The three leading EOF modes account for 56.8% of the inter-member SLP trend variance and are well separated from subsequent modes according to the criterion of North et al. (1982). These leading modes are dominated by centers of action over the Northern Hemisphere (not shown). Specifically, EOF1 exhibits an Arctic Oscillation (AO, Thompson and Wallace, 1998) like pattern, with opposite SLP anomalies over the Arctic region and northern mid-latitudes. EOF2 bears resemblance to the East Atlantic pattern (EA, Wallace and Gutzler, 1981), with a dominant action center over western Eurasia. EOF3 features a Western Pacific (WP, Wallace and Gutzler, 1981) like pattern, with a dominant action center over the Kamchatka Peninsula. In addition, similar results can be obtained from an EOF analysis over the northern extratropical domain (20º-80ºN), indicating SLP variations in boreal winter are dominated by large-scale circulation anomalies in the northern extratropics.

The three orthogonal SLP trend predictors are subsequently determined for wind trends and are removed to obtain the dynamically adjusted wind trend for individual ensemble members. By partially removing the circulation-induced component of internal variability, the dynamically adjusted trends in M02 and M28 (Fig. 6) are more comparable to the EnM trend, with the pattern correlation between M02 (M28) and EnM increasing slightly from 0.91 (0.71) for the total trend to 0.93 (0.75) for the adjusted trend. The similarity between the adjusted M02 and M28 trends is also

higher than that of the corresponding total trends (cf. Fig.6 with top panels in Fig.5), with the correlation between the two patterns increasing from 0.69 for the total trend to 0.77 for the adjusted trend. In addition, the dynamically adjusted wind trends for the 50 ensemble members are compared to the EnM (Fig.4, right). The pattern correlations between each member and EnM range from 0.75 to 0.93, with a mean of 0.88 that is higher than the mean of the total trend (0.83). The mean square difference between each member and EnM for the adjusted trend is also lower than that of the total trend (Fig. 4). The above results confirm that the spread in wind projections is partially due to the large-scale circulation-induced internal variability.

d. Influence of air temperature on the wind trend

Motion in the atmosphere is governed by the pressure gradient force, the Coriolis force, the friction force, as well as the gravitational force for vertical motion. One driving force of surface wind is air temperature because SAT changes can affect surface pressure gradients and hence wind changes (e.g., Solomon et al., 2007). This can be illustrated by the geostrophic wind approximation, as indicated in Eqs. (3) - (4). Fig. 7 displays the normalized geostrophic wind speed trend and its zonal and meridional components, calculated from the ensemble mean of SAT trends over 2021-2070. We normalize the geostrophic wind speed trend and its horizontal components by the climatological mean geostrophic wind speed over 1951-2000 at each grid box. The normalized geostrophic wind trend tends to be dominated by its zonal component, indicating that the contribution from the meridional temperature gradient is generally higher than the zonal temperature gradient, especially in northern mid-latitudes. In addition, the pattern of geostrophic wind trend bears resemblance to the CanESM5 simulated wind trend pattern, with considerable spatial variations (cf. top left in Fig.7 with top left in Fig.3). An interhemispheric asymmetry, featured by broad decreases of geostrophic wind in most of northern mid-latitude regions and increases across most of tropical and southern subtropical regions, is also evident (Fig.7, top left

and zonal averages in right panels). The similarity in the trends of simulated and geostrophic winds indicates the important driving force of air temperature on projected wind changes.

Here we analyze idealized geostrophic wind changes that are attributed to future projected SAT changes. It is noted that the geostrophic wind is a good approximation that typically appears above boundary layer (about 1-2km) in mid-latitudes. However, the geostrophic balance does not apply near the surface where winds are highly influenced by the friction resistance. Additionally, the geostrophic wind does not occur in tropical latitudes where the Coriolis force is weak.

4. Surface extreme wind

a. Climatological mean

Based on its definition, the climatological mean extreme wind index U90 over the 1980-2014 period is close to 10% for the ERA5 reanalysis (not shown). The corresponding EnM of climate simulations over the same period also shows values around 10% (Fig.8, left). The climatological mean is slightly different from 10% in the EnM, which is mainly due to climate differences between the base period 1961-1990 employed to define the simulated U90 and the period 1980-2014 considered here and to daily wind variability. We have also compared the relative agreement of the climatological mean U90 patterns for individual members to the EnM. Considerable differences are apparent in spatial correlation and variance of the U90 pattern. The pattern correlations reveal a wide range from 0.28 to 0.78 across the 50 members, and the ratios of each member to EnM variance range from 175-245% (Fig.8, right). This indicates large uncertainties in simulating spatial pattern and magnitude of the extreme wind, and suggests the internal climate variability tends to influence extreme wind U90 more than mean wind U (cf. right panel in Fig.8 with bottom right panel in Fig.2).

b. Projected trend

Figure 9 (top left) displays the ensemble mean trend of DJF mean U90 over 2021-2070. The spatial distribution of the extreme wind trend resembles that of the normalized seasonal mean wind trend (cf. top left in Fig.9 with top left in Fig.3). Nevertheless, reductions of U90 tend to be more consistent over northern mid-latitudes than reductions of mean surface wind. This is also evident in relatively weak variations of the zonal average U90 trend across northern mid-latitudes (Fig.9, top right). Consequently an interhemispheric asymmetry, featured by U90 decreases over northern mid-latitude regions and increases broadly across tropical and southern subtropical regions, is also found (Fig.9, top right). In addition, the inter-member variability of the U90 trend is about 1.0-2.5%/50yr over most regions, except high variances exceeding 3.0%/50yr over norther parts of South America, south of West Africa, and Angola (Fig.9, middle panels). The signal-to-noise ratio pattern (Fig.9, bottom panel) also resembles the EnM U90 trend.

The similarity of the extreme wind trends across the 50 ensemble members is illustrated by high pattern correlations between individual members and EnM (0.86-0.93, left panel in Fig. 10). Meanwhile, individual simulations exhibit slightly higher spatial variances than the EnM variance, with the variance ratio below 125%. The mean square difference between each member and the EnM is below 30%. The good correspondence across the 50 members indicates a relatively stable U90 change. Hence, the interhemispheric asymmetry of extreme wind changes as described above can be expected in the next half-century, although large uncertainties are seen in the climatological mean U90 in individual simulations.

c. Internally generated and dynamically adjusted trends

The extreme wind trend is also decomposed into externally anthropogenic forced and internal climate variability generated components. Figure 11 displays the total and internally generated U90 trends for the two members that have the highest (r=0.93; member 37, M37) and lowest (r=0.86; member 01, M01) pattern correlations with the EnM. The two members exhibit broadly similar

structure of total trend compared to the EnM, as well as the interhemispheric asymmetry feature in both cases (Fig.11, top panels). The pattern correlation of total trend between M37 and M01 is 0.80. The discrepancy between them is mainly in magnitude of the trend, except opposite trends over northeastern China and patches of small areas. M01 depicts increases of U90 over northeastern China, which is opposite to those in M37 and EnM. The difference is also evident in the internally generated trend (Fig. 13, bottom panels), which shows large-scale spatial coherence over land. In addition, the internally generated trend is comparable to the forced trend, especially over action centers of the internal trend in northern mid-high latitudes, and hence contributes to the total trend.

Given the relationship between the large-scale circulation variability and synoptic-scale atmospheric variations (e.g., Wallace and Gutzler, 1981; Vose et al., 2014; Yu et al., 2019), we also remove influences of the three leading SLP trend predictors, as described in last section, to obtain a dynamically adjusted extreme wind trend. By partially reducing the contribution of the large-scale circulation-induced component in the extreme wind trend, increases of U90 over northeastern China in M01 are weaker in the adjusted trend than total trend (Fig.12). Meanwhile, the pattern correlation of the adjusted trend between M01 and M37 is 0.85, slightly higher than that of the total trend (0.80). In addition, the pattern correlation between M01 and EnM increases from 0.86 for the total trend to 0.91 for the adjusted trend, and increases slightly from 0.93 to 0.94 between M37 and EnM. The right panel of Fig. 10 further compares the spatial pattern correlation and variance for individual members to the EnM for the adjusted U90 trend. The pattern correlations range from 0.88 to 0.95, with a mean of 0.93 that is slightly higher than the mean of total trend (0.91). In addition, the ratio of individual member to EnM variances and the mean square difference between each member and EnM for the adjusted trend are also slightly lower than the counterparts of total trend. Overall, the spread in U90 projections decreases by partially removing the large-scale atmospheric circulation variability.

5. Summary and discussion

Based on a 50-member SMILE of climate simulations generated by CanESM5, we analyze the ensemble mean and spread of future projections of global surface mean and extreme winds in boreal winter. The simulations are forced by historical anthropogenic and natural forcings over 1850-2014 and the SSP5-8.5 high-emissions scenario over 2015-2100. To evaluate the performance of CanESM5, modelled surface winds in the historical simulation over 1980-2014 are compared to the corresponding ERA5 reanalysis result. The projected wind trends over the next half-century are subsequently analyzed using the climate change simulation over 2021-2070. We examine the externally anthropogenic forced and internal climate variability generated components of projected surface mean and extreme wind trends, and explore the influence of large-scale atmospheric circulation-induced variability on these trends. The main findings can be summarized as follows.

1) CanESM5 can reasonably well simulate the ERA5 based surface wind speed pattern, with differences mainly over regions of high topographies. The discrepancy may be partially attributed to different grid resolutions of the climate and reanalysis models, which influence the land-surface roughness and elevation representation.

2) Surface wind speed over the next half-century is projected to mostly decrease in northern mid-low latitudes and southern mid-latitudes and increase in northern high latitudes and southern tropical and subtropical regions, with considerable regional variations. The broad reduction over northern mid-latitude regions and increase across tropical and southern subtropical regions feature an interhemispheric asymmetry. The driving force of air temperature plays an important role in the projected wind change. The interhemispheric asymmetry of wind projections is apparent in most ensemble members, with remarkable differences over northern parts of South America and northern Russia.

3) The projected extreme wind change resembles the mean surface wind change. However, reductions of the extreme wind tend to be more consistent over northern mid-latitudes. The interhemispheric asymmetry of future extreme wind changes is found in all ensemble members, although large uncertainties are evident in the climatological mean of extreme wind in individual simulations.

4) The projected surface mean and extreme wind changes are attributed to changes in both externally anthropogenic forced and internal climate variability generated wind components. The internally generated wind trend reveals large-scale spatial coherence, similar to the feature previously found in temperature projections. The spread in surface wind projections is partially due to large-scale atmospheric circulation variability.

Extreme wind projections reported here are based on an index defined with the percentage of time when daily wind speed is above its 90^{th} percentile. Similar projected results can be obtained using an index defined with daily maximum wind speed. Fourth order polynomial curves are employed to schematically illustrate the projected SAT change and zonally averaged wind trend. The interhemispheric asymmetry of wind projections is also evident if the fifth order polynomial fitting is applied. Nevertheless, robustness of the asymmetry feature remains to be explored in other CMIP6 climate simulations. In addition, the dynamically adjusted approach we utilized to consider large-scale circulation-induced variability on surface wind projections is similar to adjustments by means of partial least squares regressions applied in temperature and precipitation studies (e.g., Wallace et al., 2014; Deser et al., 2014; Hu et al., 2019), and differs from the adjusted method based on constructed atmospheric circulation analogs (e.g., Deser et al., 2016; Gong et al., 2019). Regional-scale and synoptic-scale circulation variability can also influence wind variations, especially for extreme winds. How and to what extent various spatial and temporal scale climate variability impacts surface wind projections remain to be investigated.

Acknowledgments We thank colleagues at the CCCma in producing the climate simulations analyzed here. Data used in this study are described in section 2.

Figures

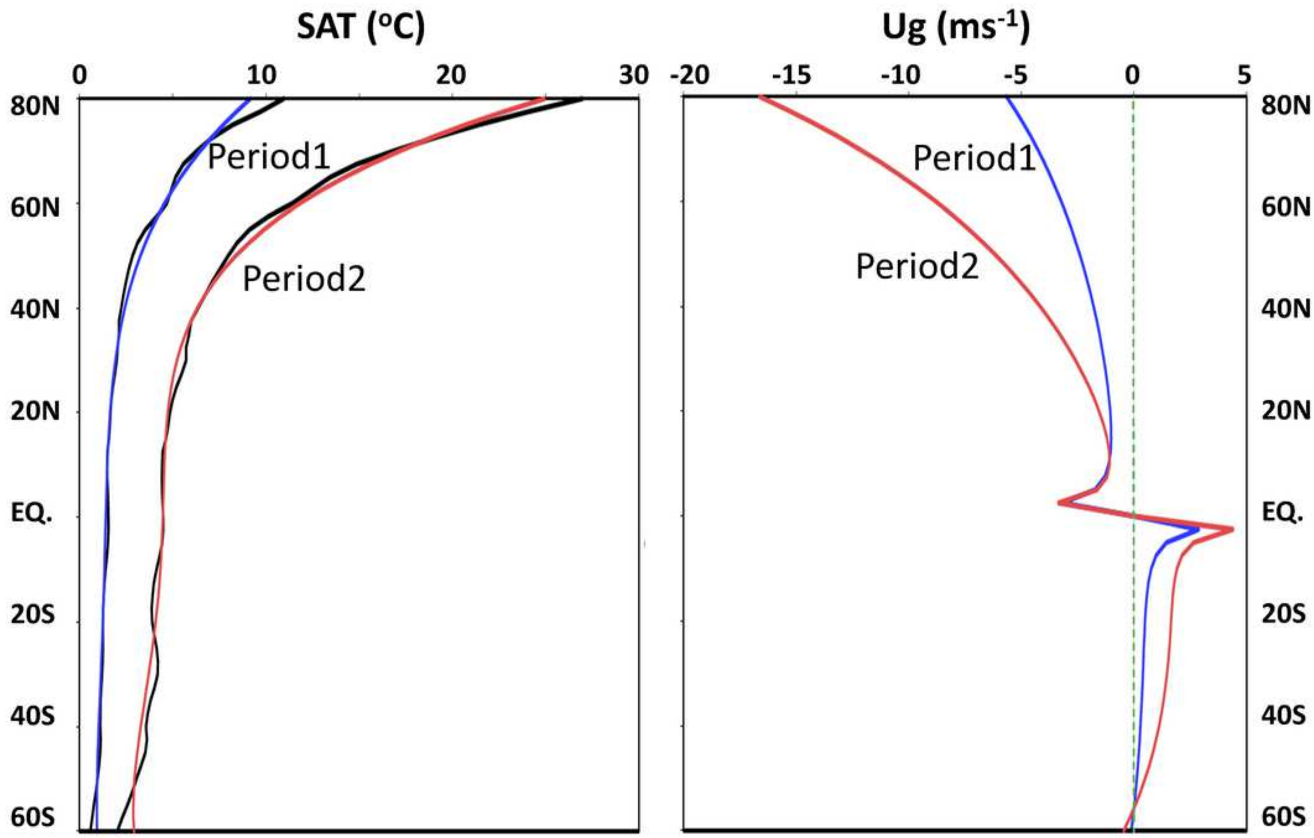

Figure 1

Zonal averages of DJF mean SAT changes (left, unit oC) for the period 1 of 2001-2050 relative to 1951-2000 and period 2 of 2051-2100 relative to 1951-2000, together with a quartic fit to each zonal average. Geostrophic wind approximations (right, unit ms-1) for the two periods, calculated from the quartic fit curves of SAT changes.

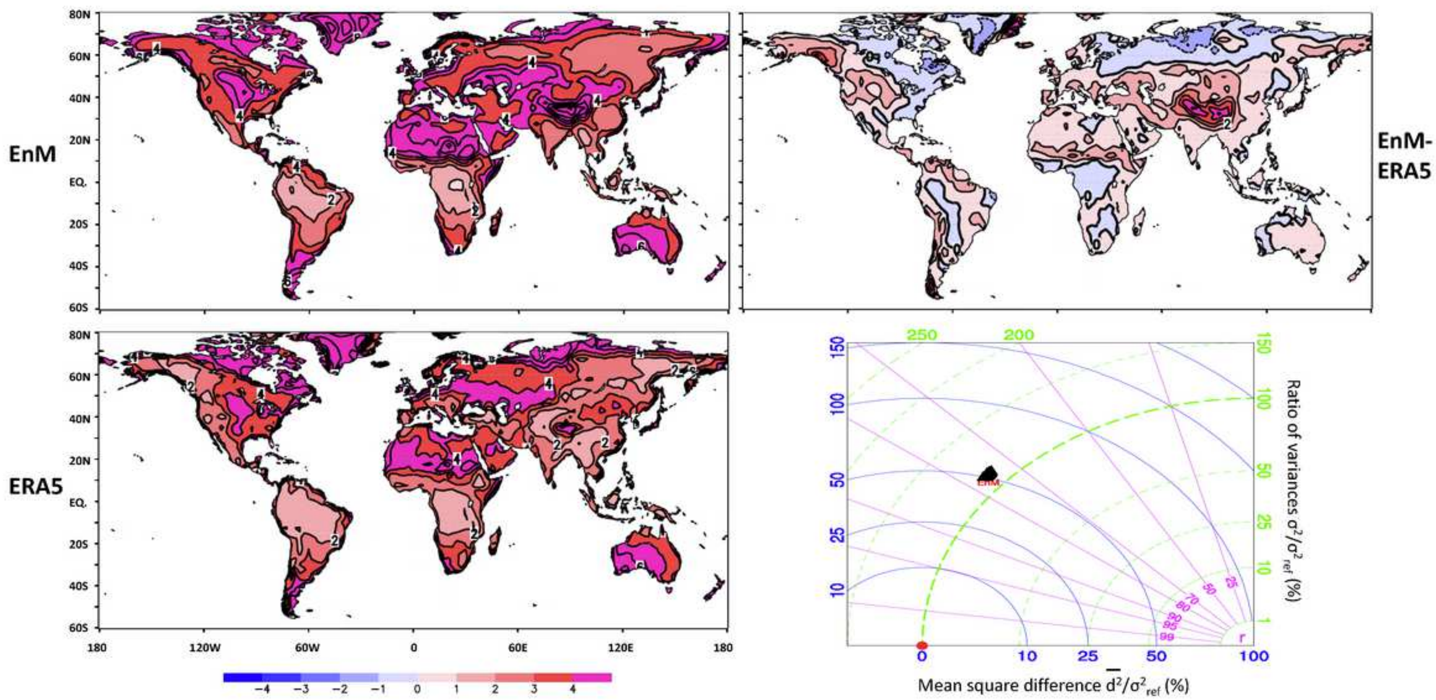

Figure 2

DJF climatological means of surface wind speed over the 1980-2014 period for the EnM of CanESM5 simulations (top left), ERA5 reanalysis (bottom left), and difference between them (EnM-ERA5, top right). Contour interval is 1.0ms-1. The thick black line indicates the zero line. BLT diagram (bottom right) illustrating the pattern correlation (magenta), the ratio of model to reanalysis variance (green), and the relative mean square difference (blue) between each simulation and reanalysis results of DJF climatological mean winds over 1980-2014, in unit percentage. The EnM result is also shown. Note: The designations employed and the presentation of the material on this map do not imply the expression of any opinion whatsoever on the part of Research Square concerning the legal status of any country, territory, city or area or of its authorities, or concerning the delimitation of its frontiers or boundaries. This map has been provided by the authors.

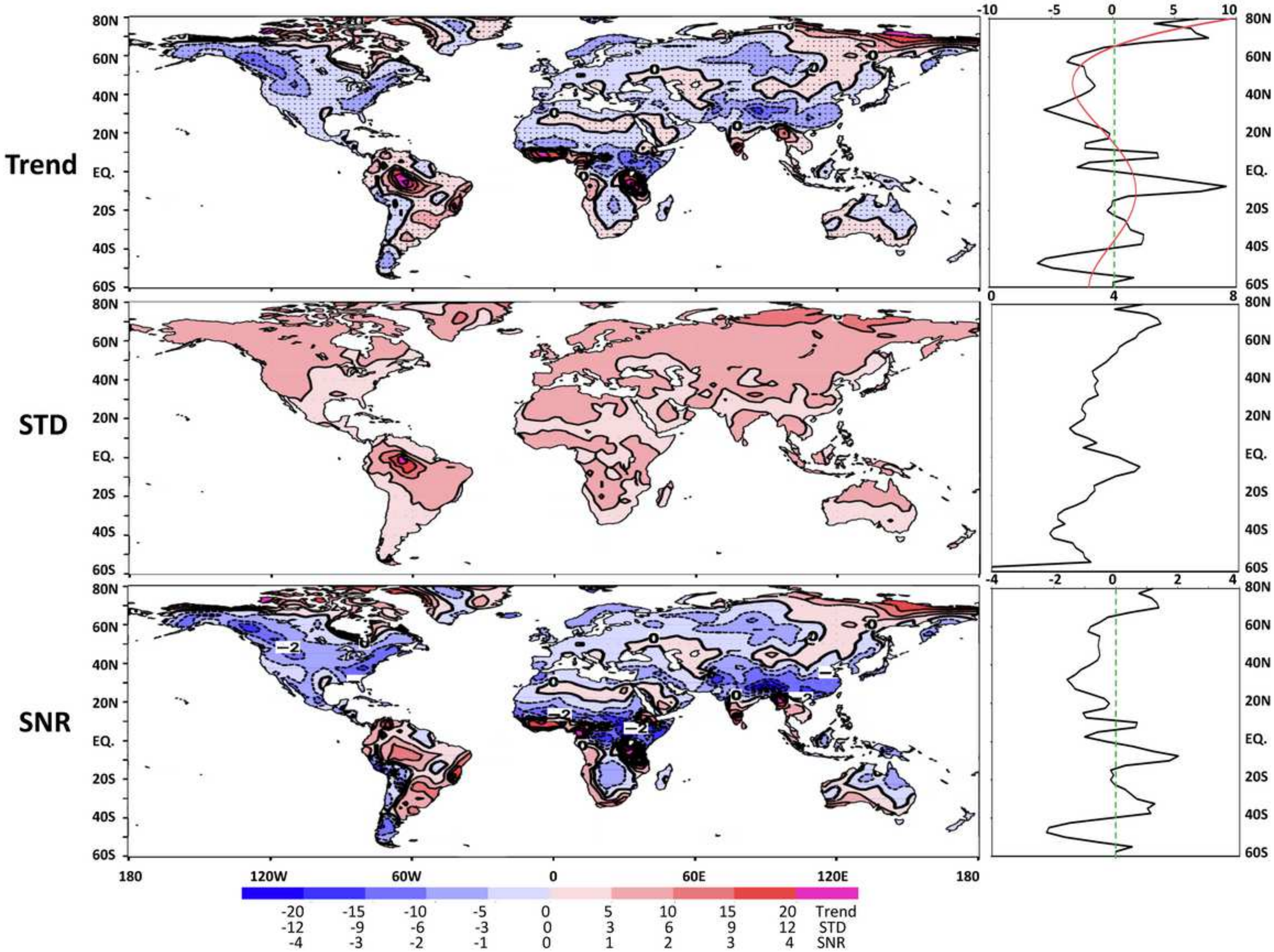

Figure 3

Normalized wind speed trends over 2021-2070 (top left, interval 5.0%/50yr) for the ensemble mean. Stippling regions indicate trends significant at the 95% confidence level. Standard deviation (middle left, interval 3.0%/50yr) and signal-to-noise ratio (bottom left, interval 1.0) of the normalized wind speed trends among the 50 ensemble members. The thick black line indicates the zero line. Zonal averages of the trend (superimposed by a quartic fit in red), standard deviation and signal-to-noise ratio are shown from the top right to the bottom right. Note: The designations employed and the presentation of the material on this map do not imply the expression of any opinion whatsoever on the part of Research Square concerning the legal status of any country, territory, city or area or of its authorities, or concerning the delimitation of its frontiers or boundaries. This map has been provided by the authors.

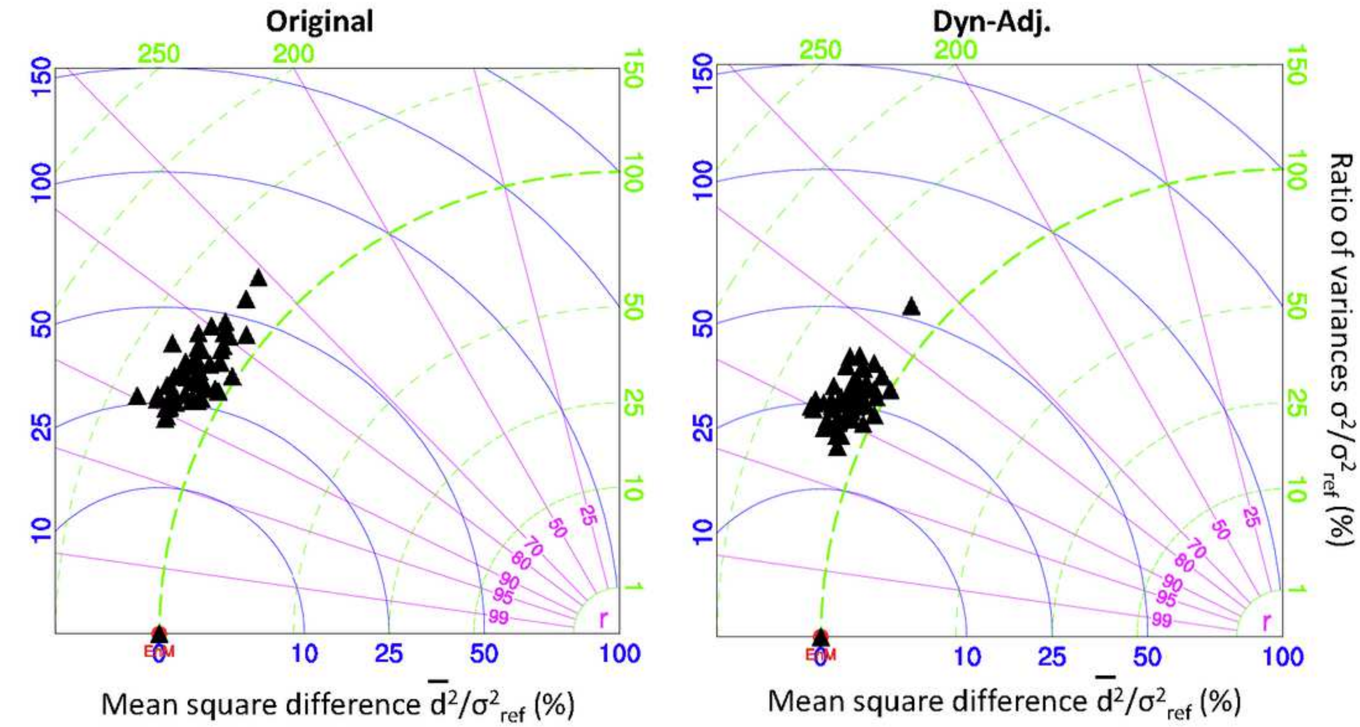

Figure 4

(left) BLT diagram illustrating the pattern correlation, the ratio of model to EnM variance, and the relative mean square difference between each simulation and the EnM values of normalized wind trends over the 2021-2070 period, in unit percentage. (right) As in left, but for the corresponding dynamically adjusted results.

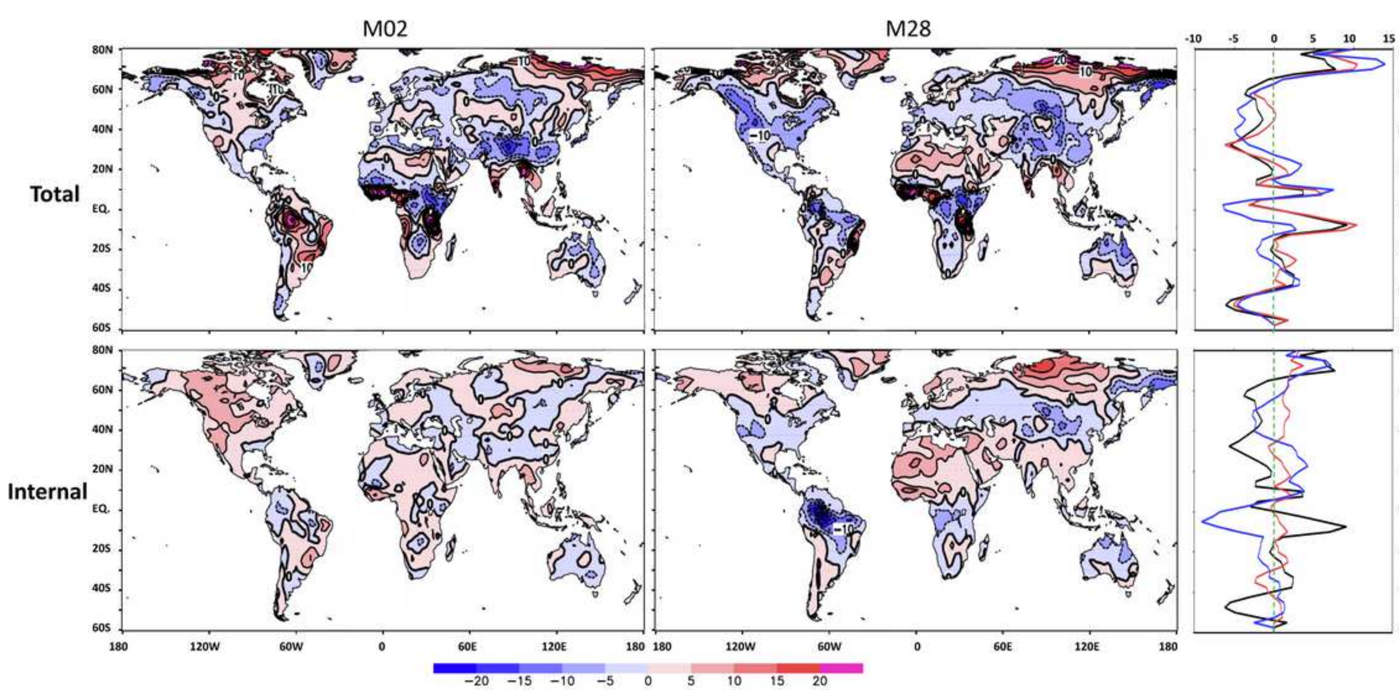

Figure 5

Total (top row) and internal components (bottom row) of the normalized wind speed trends over 2021-2070 for member 02 (left column) and member 28 (middle column). Contour interval is 5.0%/50yr. The thick black line indicates the zero line. (top right) Zonal averages of the total trend for the EnM (black), M02 (red), and M28 (blue). (bottom right) Zonal averages of the total trend for the EnM (black) and of the internal trend for M02 (red) and M28 (blue). Note: The designations employed and the presentation of the material on this map do not imply the expression of any opinion whatsoever on the part of Research Square concerning the legal status of any country, territory, city or area or of its authorities, or concerning the delimitation of its frontiers or boundaries. This map has been provided by the authors.

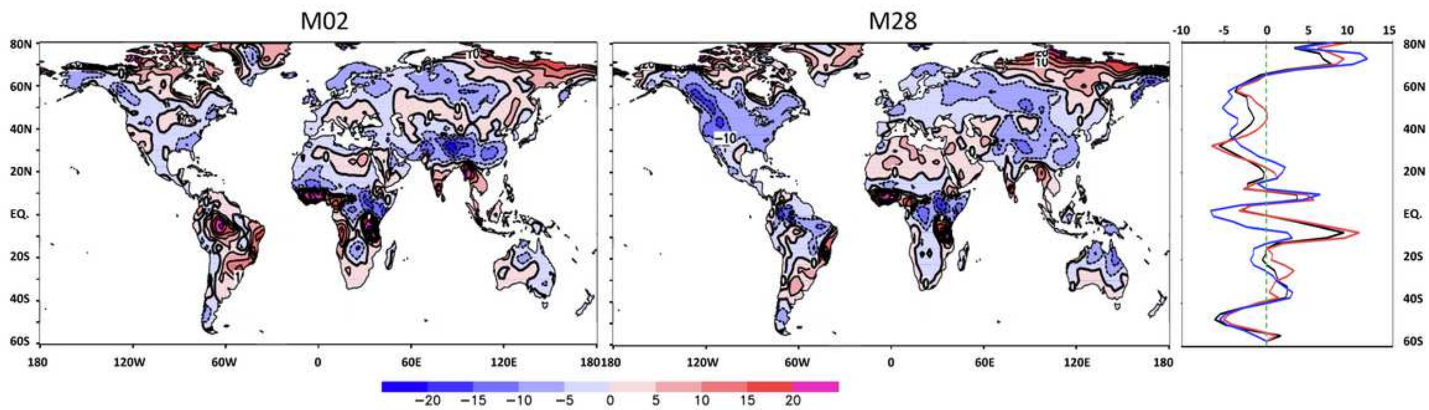

Figure 6

Dynamically adjusted components of the normalized wind speed trends for member 02 (left) and member 28 (middle). Contour interval is 5.0%/50yr. The thick black line indicates the zero line. (right) Zonal averages of the total trend for the EnM (black) and of the adjusted trend for M02 (red) and M28 (blue). Note: The designations employed and the presentation of the material on this map do not imply the expression of any opinion whatsoever on the part of Research Square concerning the legal status of any country, territory, city or area or of its authorities, or concerning the delimitation of its frontiers or boundaries. This map has been provided by the authors.

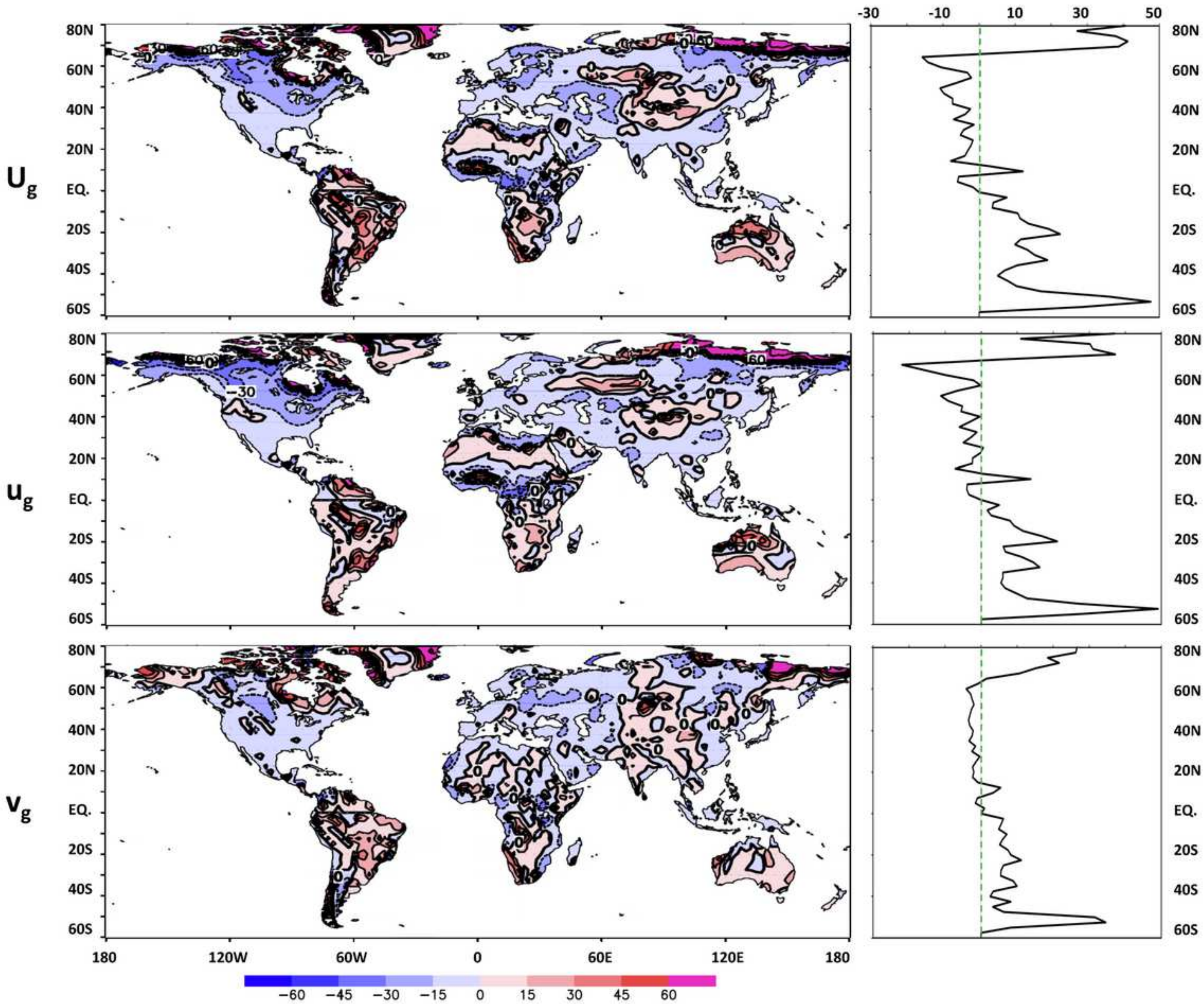

Figure 7

Normalized geostrophic wind speed trend (top left) and its zonal (middle left) and meridional (bottom left) components, calculated from the SAT trend over 2021-2070. Contour interval is 5.0%/50yr. The thick black line indicates the zero line. Zonal averages of the normalized geostrophic wind speed trend and its zonal and meridional components are shown from the top right to the bottom right. Note: The designations employed and the presentation of the material on this map do not imply the expression of any opinion whatsoever on the part of Research Square concerning the legal status of any country, territory, city or area or of its authorities, or concerning the delimitation of its frontiers or boundaries. This map has been provided by the authors.

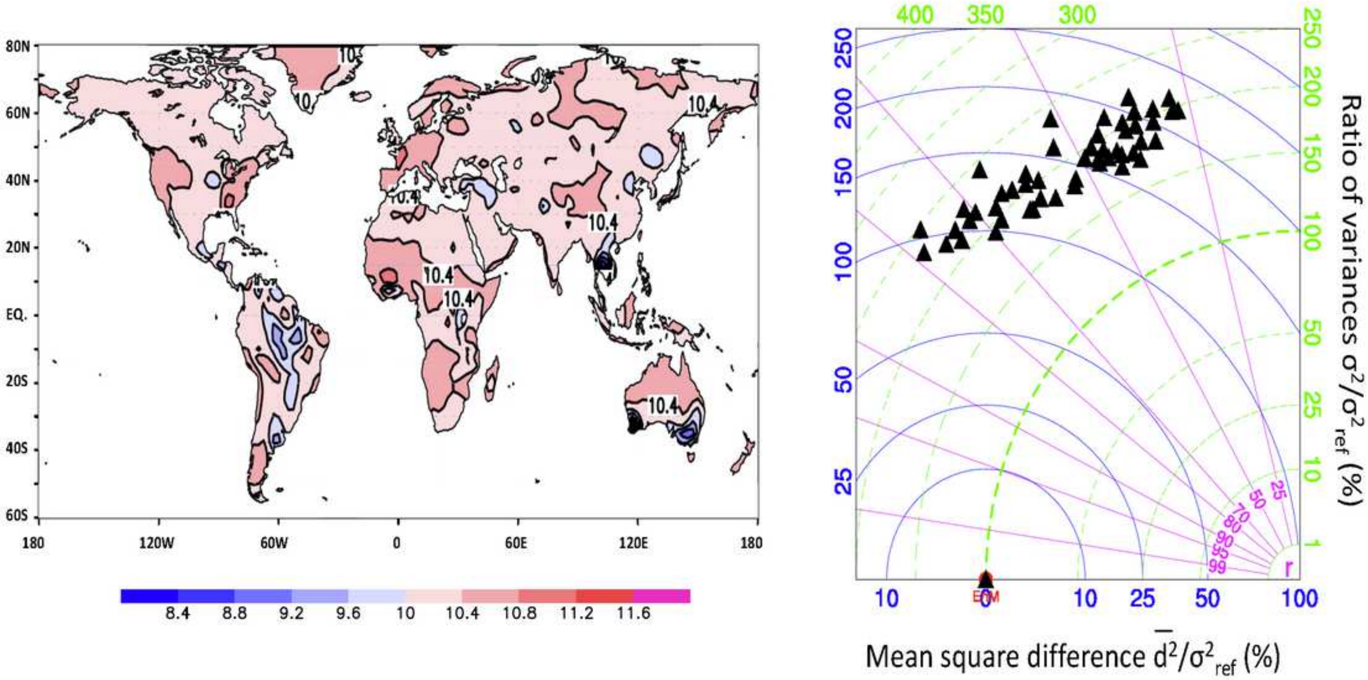

Figure 8

DJF climatological mean of the extreme wind index over the 1980-2014 period for the EnM of CanESM5 simulations (left, interval 0.4%). BLT diagram (right) displaying the pattern correlation, the ratio of model to EnM variance, and the relative mean square difference between each simulation and the EnM values of DJF climatological mean extreme wind indices over 1980-2014, in unit percentage. Note: The designations employed and the presentation of the material on this map do not imply the expression of any opinion whatsoever on the part of Research Square concerning the legal status of any country, territory, city or area or of its authorities, or concerning the delimitation of its frontiers or boundaries. This map has been provided by the authors.

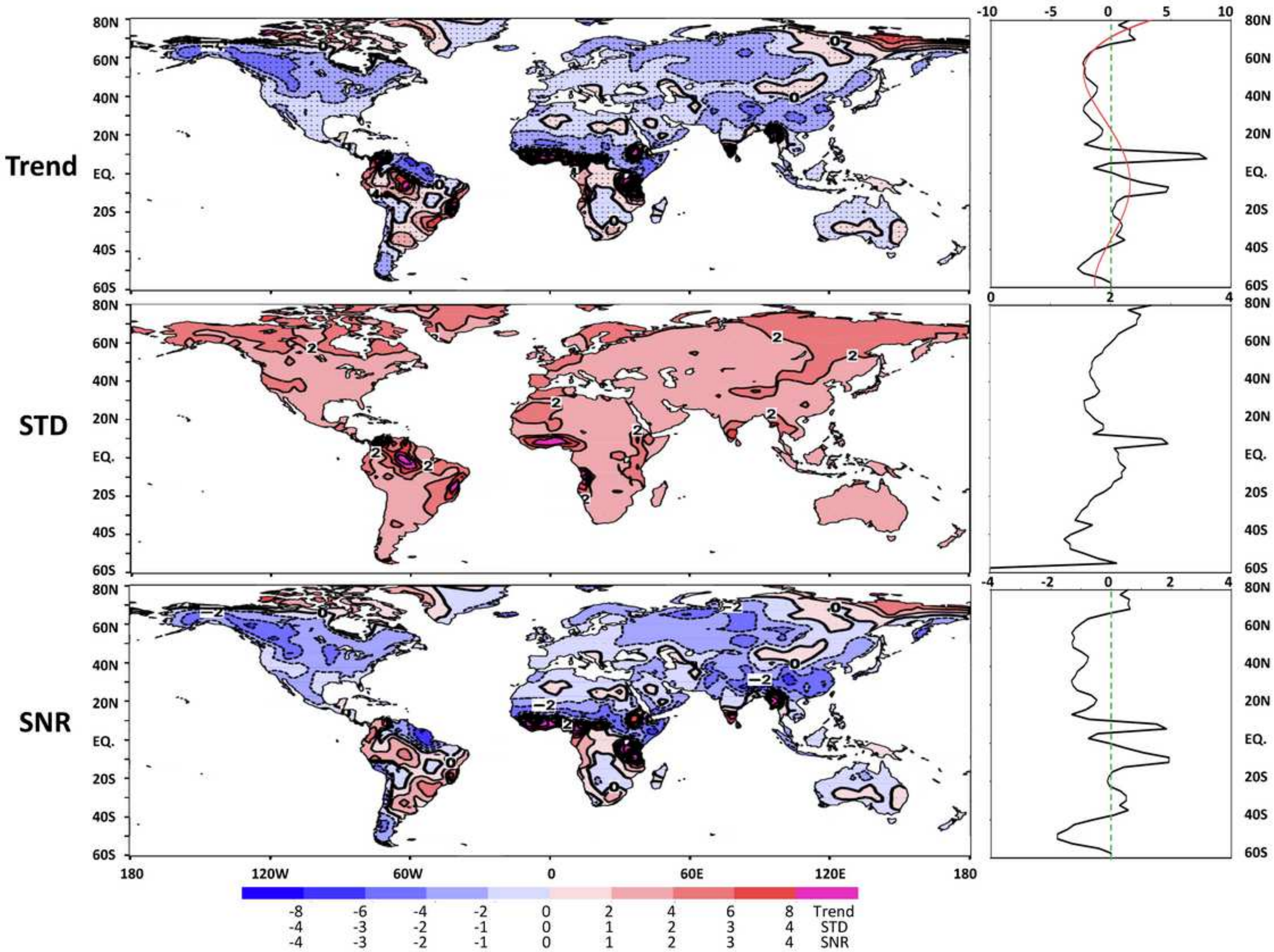

Figure 9

As in Fig.3, but for the extreme wind trend. Contour intervals are 2.0%/50yr for the trend, and 1.0%/50yr for the standard deviation. Note: The designations employed and the presentation of the material on this map do not imply the expression of any opinion whatsoever on the part of Research Square concerning the legal status of any country, territory, city or area or of its authorities, or concerning the delimitation of its frontiers or boundaries. This map has been provided by the authors.

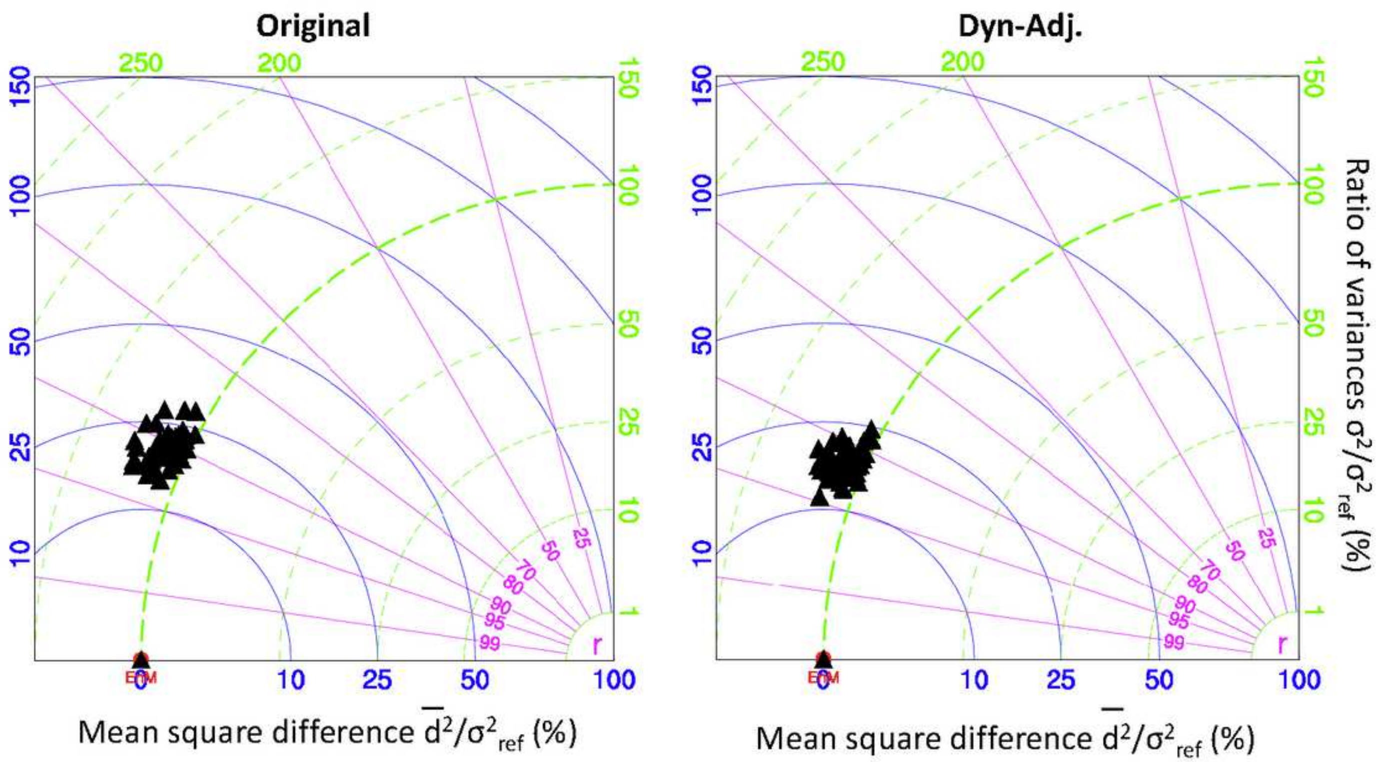

Figure 10

As in Fig.4, but for the extreme wind trend.

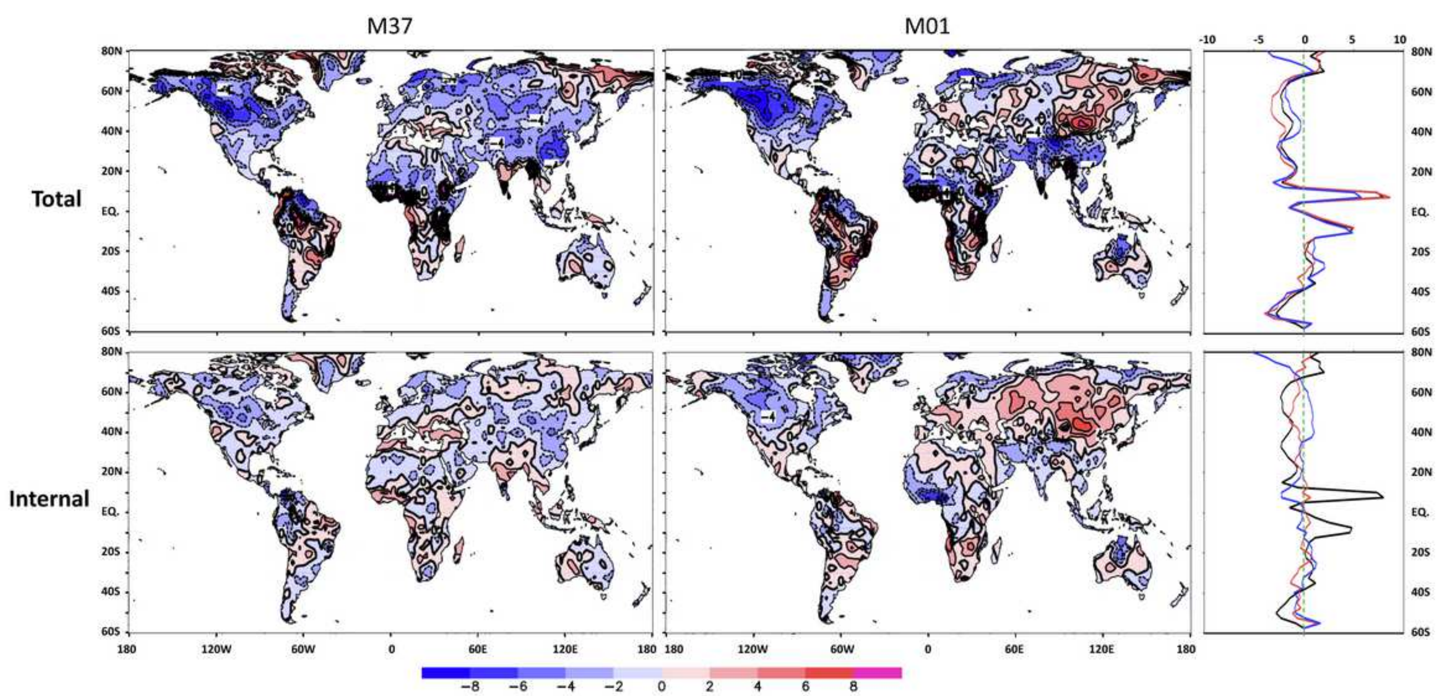

Figure 11

As in Fig.5, but for the extreme wind trends of member 37 (left column) and member 01 (middle column) with contour interval 2.0%/50yr. Note: The designations employed and the presentation of the material on this map do not imply the expression of any opinion whatsoever on the part of Research Square concerning the legal status of any country, territory, city or area or of its authorities, or concerning the delimitation of its frontiers or boundaries. This map has been provided by the authors.

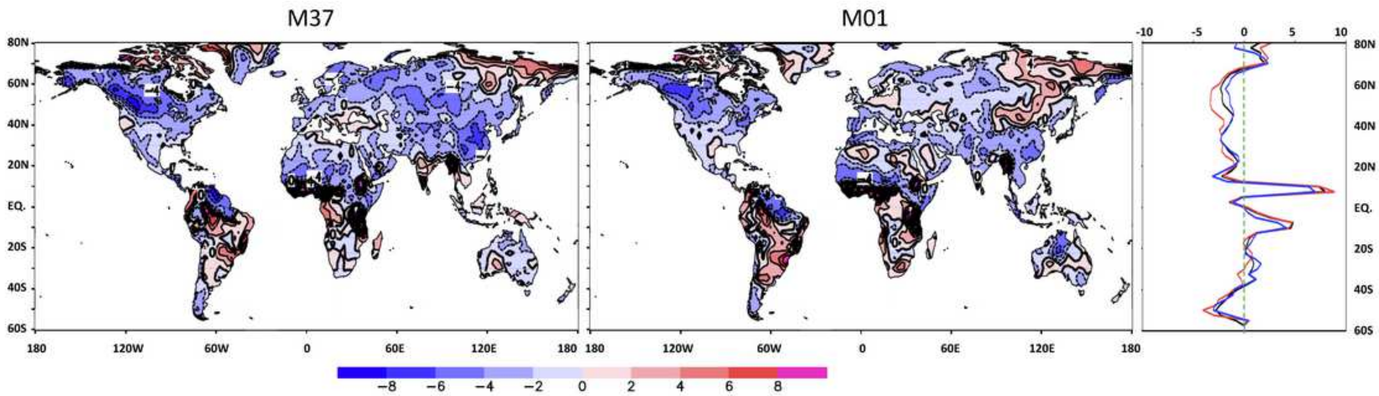

Figure 12

As in Fig.6, but for the extreme wind trends of member 37 (left) and member 01 (middle) with contour interval 2.0%/50yr. Note: The designations employed and the presentation of the material on this map do not imply the expression of any opinion whatsoever on the part of Research Square concerning the legal status of any country, territory, city or area or of its authorities, or concerning the delimitation of its frontiers or boundaries. This map has been provided by the authors.

Supplementary Files

This is a list of supplementary files associated with this preprint. Click to download.

- references.pdf